

The i-process yields of rapidly-accreting white dwarfs from multicycle He-shell flash stellar evolution models with mixing parameterizations from 3D hydrodynamics simulations

Pavel A. Denissenkov,^{1,2,†*} Falk Herwig,^{1,2,†} Paul Woodward,^{2,3} Robert Andrassey,^{1,2} Marco Pignatari^{2,4,5,†} and Samuel Jones^{6,†}

¹*Department of Physics and Astronomy, University of Victoria, Victoria, BC, V8W 2Y2, Canada*

²*Joint Institute for Nuclear Astrophysics - Center for the Evolution of the Elements, USA*

³*LCSE and Department of Astronomy, University of Minnesota, Minneapolis, MN 55455, USA*

⁴*E.A. Milne Centre for Astrophysics, Department of Physics & Mathematics, University of Hull, HU6 7RX, United Kingdom*

⁵*Konkoly Observatory, Research Centre for Astronomy and Earth Sciences, Hungarian Academy of Sciences, Konkoly-Thege, Miklós út 15-17, H-1121 Budapest, Hungary*

⁶*Computational Physics and Methods (CCS-2) and Center for Theoretical Astrophysics, Los Alamos National Laboratory, NM 87544, USA*

[†]*NuGrid Collaboration, <http://nugridstars.org>*

Accepted XXX. Received YYY; in original form ZZZ

ABSTRACT

We have modelled the multicycle evolution of rapidly-accreting CO white dwarfs (RAWDs) with stable H burning intermittent with strong He-shell flashes on their surfaces for $0.7 \leq M_{\text{RAWD}}/M_{\odot} \leq 0.75$ and $[\text{Fe}/\text{H}]$ ranging from 0 to -2.6 . We have also computed the i-process nucleosynthesis yields for these models. The i process occurs when convection driven by the He-shell flash ingests protons from the accreted H-rich surface layer, which results in maximum neutron densities $N_{\text{n,max}} \approx 10^{13} - 10^{15} \text{ cm}^{-3}$. The H-ingestion rate and the convective boundary mixing (CBM) parameter f_{top} adopted in the one-dimensional nucleosynthesis and stellar evolution models are constrained through 3D hydrodynamic simulations. The mass ingestion rate and, for the first time, the scaling laws for the CBM parameter f_{top} have been determined from 3D hydrodynamic simulations. We confirm our previous result that the high-metallicity RAWDs have a low mass retention efficiency ($\eta \lesssim 10\%$). A new result is that RAWDs with $[\text{Fe}/\text{H}] \lesssim -2$ have $\eta \gtrsim 20\%$, therefore their masses may reach the Chandrasekhar limit and they may eventually explode as SNeIa. This result and the good fits of the i-process yields from the metal-poor RAWDs to the observed chemical composition of the CEMP-r/s stars suggest that some of the present-day CEMP-r/s stars could be former distant members of triple systems, orbiting close binary systems with RAWDs that may have later exploded as SNeIa.

Key words: Sun: abundances — process: nucleosynthesis — stars: binaries — Galaxy: abundances

1 INTRODUCTION

The type Ia supernovae (SNeIa) are thermonuclear explosions of carbon-oxygen (CO) white dwarfs (WDs) (e.g. Hoyle & Fowler 1960; Hillebrandt & Niemeyer 2000; Hillebrandt et al. 2013; Churazov et al. 2014; Livio & Mazzali 2018). In

the single degenerate (SD) channel of SNeIa progenitors, that was originally proposed by Schatzman (1963) and Whelan & Iben (1973), it is assumed that the CO WD is a primary star of a close binary system with a main-sequence, sub-giant or red-giant-branch companion. The secondary star fills its Roche lobe and donates matter from an H-rich envelope to the WD, and, as a result, the WD will explode when its growing mass M_{WD} approaches the Chandrasekhar limit

* E-mail: pavelden@uvic.ca

$M_{\text{Ch}} \approx 1.38 M_{\odot}$. Initially, the primary star of such a binary system was an intermediate-mass star with $M \approx 2.5 - 7 M_{\odot}$, the upper boundary of this mass interval depending on the amount of convective boundary mixing and C-burning rate (Chen et al. 2014). It left a core — the CO WD — after having lost the rest of its mass during a common-envelope event, when it arrived at the asymptotic-giant branch (AGB) and filled its Roche lobe. Given that the CO cores of AGB stars can grow in mass only up to $\sim 1 M_{\odot}$ (Chen et al. 2014), the SD channel can work only if the accreted H-rich matter is first processed into He and then into C and O, while being efficiently retained on the WD.

Figure 9 of Nomoto (1982) summarizes the results of the previous investigations of H accretion onto CO WDs at different rates \dot{M}_{acc} (an update of this figure can be found in Nomoto et al. 2007). It shows that stable burning of accreted H occurs in a very narrow interval of \dot{M}_{acc} around a value of $\sim 10^{-7} M_{\odot} \text{ yr}^{-1}$ that linearly increases with M_{WD} . At the lower rates, H is processed into He via thermal flashes that become stronger when \dot{M}_{acc} decreases, eventually leading to thermonuclear runaways typical for the classical novae. At the higher rates, the non-processed H accumulates in an expanding envelope, so that such a rapidly accreting WD would be resembling a red giant.

However, an important aspect of the evolution of rapidly accreting white dwarfs is the fact that even if accreted H is burning stably the He shell will ignite in a thermonuclear runaway when enough He has been accumulated as H-shell burning ash, just as in a thermal-pulse AGB star (Cassisi et al. 1998). A few consecutive He-shell flashes at the end of H accretion were computed by Idan et al. (2013). Following Nomoto (1982), various outcomes of pure He accretion onto CO WDs at different values of \dot{M}_{acc} have been studied in a number of papers (e.g. Piersanti et al. 2014; Wang et al. 2015). The data obtained in such simulations are used in models of binary population synthesis to estimate a theoretical SNIa rate for the SD channel, simply assuming that the He accretion rate matches that of H in the regime of stable H burning (e.g. Han & Podsiadlowski 2004).

Recently, Denissenkov et al. (2017a, hereafter Paper I) have presented the results of the first stellar evolution computations in which rapid accretion and stable burning of H on CO WDs were repeatedly interrupted by strong He-shell flashes that were followed by mass loss caused either by the super-Eddington luminosity wind or by the common-envelope event resulting from the expansion of the WD envelope overflowing its Roche lobe, after which the H accretion resumed. These simulations show a low efficiency of He retention ($\eta_{\text{He}} \lesssim 10\%$) and, because all the processes that accompany the rapid H accretion were taken into account, they provide estimates of the low retention efficiency of the total accreted mass ($\eta \approx \eta_{\text{He}}$) by the rapidly-accreting WDs (RAWDs)¹. In one of the models even a negative value of η_{He} was found meaning that M_{WD} was decreasing with time. Given that the binary population synthesis models predict

an order of magnitude lower SNIa rates for the SD channel when optimistically assuming that $\eta_{\text{He}} = 100\%$, this result of Paper I makes the SD channel highly unlikely. Fortunately, there are a number of alternative channels of SNIa progenitors, various pros and cons of which are discussed by Wang (2018) and Livio & Mazzali (2018).

Paper I has proposed a new application for the former SD channel, namely, instead of growing in mass towards M_{Ch} and exploding as SNeIa, the RAWDs could be a stellar site of the intermediate (i) process of neutron captures by heavy isotopes (Cowan & Rose 1977). This idea is based on the similarity of physics that one encounters in the RAWD models and in the model of the post-AGB star Sakurai's object (V4334 Sagittarii) in which the elemental abundance signature of the i-process nucleosynthesis was observed by Asplund et al. (1999) and interpreted by Herwig et al. (2011). Indeed, in both cases the He-shell burning drives convection that ingests protons from an H-rich envelope. This triggers the reactions $^{12}\text{C}(p, \gamma)^{13}\text{N}$, $^{13}\text{N}(e^+ \nu)^{13}\text{C}$ and $^{13}\text{C}(\alpha, n)^{16}\text{O}$, the first one taking place close to the top and the third one near the bottom of the He convective zone, and ^{13}N decaying into ^{13}C while being transported downwards.

The exact mechanism of how this convective flow operates in different cases is still under investigation. Sakurai's object is believed to be a very late thermal pulse, i.e. the He-shell flash occurred when the H-burning shell of the star had already turned off and the star had evolved around the knee² in the HRD. Stellar evolution models predict an immediate split of the He-shell flash convection zone which would prevent any mixing of protons and the burning products of p capture on ^{12}C into the hottest bottom region of the pulse-driven convection zone. Herwig et al. (2014) have shown that in three-dimensional hydrodynamic simulations the H ingestion triggers a Global Oscillation of Shell H-ingestion (GOSH) which drastically rearranges the structure of the He-shell flash convection zone. So far it has not been possible to follow the long-term evolution of this event past the first GOSH. The one-dimensional, spherically symmetric nucleosynthesis simulations of Herwig et al. (2011) adopted the approach that mixing between the upper layer in which protons and ^{12}C react and the bottom layer in the pulse-driven convection zone, where neutrons can be released via the $^{13}\text{C}(\alpha, n)^{16}\text{O}$ reaction, continues until the observed chemical composition of Sakurai's object has been reproduced as well as possible. This *delayed-split* scenario is not yet fully supported by the initial three-dimensional hydrodynamics simulation results by Herwig et al. (2014). The initial GOSH in those simulations happens at a time when the amount of protons consumed is still insufficient to explain the neutron exposure required to explain observations, and the evolution past the initial GOSH in three dimensions remains unclear.

With an ongoing supply of protons, most of which are transformed into neutrons in the above reactions, the neutron number density at the bottom of the He zone can reach a value of $N_n \sim 10^{15} \text{ cm}^{-3}$ intermediate between the values characteristic of the *s* ($N_n \lesssim 10^{11} \text{ cm}^{-3}$) and *r*

¹ We define an RAWD as a WD that accretes H rapidly enough for its stable burning to be maintained on the WD surface. This definition is slightly different from the one used by Lepo & van Kerkwijk (2013) whose RAWDs can have the higher accretion rates and lose mass via the optically thick wind.

² A segment of a WD cooling track where the evolution with nearly constant luminosity and increasing effective temperature changes to the evolution with both of them decreasing.

($N_n \gtrsim 10^{20} \text{ cm}^{-3}$) process. Very-late thermal pulse objects such as the post-AGB star Sakurai's object will only experience one H-ingestion event. Their nucleosynthesis production is very unique, but the impact on a galactic chemical evolution scale is negligible. RAWDs on the other hand continuously accrete from a close binary companion, and can potentially experience dozens of He-shell flashes followed by mass-loss episodes before the concomitant changes in the binary system parameters terminate the rapid H accretion. Along with their low mass retention efficiency, this makes the RAWDs a potentially important galactic sources of heavy elements, with distinct elemental and isotopic abundance signatures different from those produced in the *s* and *r* process. For example, *i* process from RAWDs can make a significant contribution to the first *n*-capture peak of the solar system abundance distribution, as demonstrated by combining RAWD *i*-process yields with stellar population synthesis and galactic chemical evolution models (Côté et al. 2018).

RAWDs are not the only possible sites of *i*-process nucleosynthesis triggered by H ingestion into a He convective zone. The other sites can be low-metallicity and low-mass thermally-pulsing AGB stars (Iwamoto et al. 2004; Lugaro et al. 2012), He-core flash in low-metallicity RGB stars (Campbell et al. 2010), super-AGB stars (Jones et al. 2016), and H- and He-burning shell merger in Population-III massive stars (Clarkson et al. 2018; Banerjee et al. 2018).

In Paper I, we have considered the rapid ($\dot{M}_{\text{acc}} = 1\text{--}2 \times 10^{-7} M_{\odot} \text{ yr}^{-1}$) accretion of only solar-composition matter onto CO WDs with the masses $0.65 M_{\odot}$, $0.73 M_{\odot}$ and $1 M_{\odot}$. The present work extends the set of our RAWD models to sub-solar metallicities, while keeping their masses close to $M_{\text{WD}} \approx 0.73 M_{\odot}$. The main goals of this paper are to describe the methods that we use to simulate the multicycle evolution of RAWDs (Section 2.1) and the *i*-process nucleosynthesis in their He-flash convection zones during H ingestion (Section 2.2), and to present the results of our new computations of the RAWD evolution and *i*-process yields for a range of metallicity (Section 4) that have been used in Côté et al. (2018). Section 3 describes the 3D hydrodynamic simulations that support our 1D estimates of H mass ingestion rates for the RAWD models. Section 5 concludes the paper.

2 METHODS USED FOR ONE-DIMENSIONAL STELLAR EVOLUTION AND NUCLEOSYNTHESIS SIMULATIONS

2.1 The RAWD evolution

The new RAWD models are computed with the revision 7624 of the MESA stellar evolution code (Paxton et al. 2011, 2013). We use the reaction rates from the *JINA Reaclib* database (Cyburt et al. 2010) and the MESA default equation of state. The nuclear network includes 31 species, from neutron to ^{28}Si , that can participate in 60 reactions of the pp chains, four CNO cycles, NeNa and MgAl cycles, as well as the He (triple- α , $^{12}\text{C}(\alpha, \gamma)^{16}\text{O}$, $^{16}\text{O}(\alpha, \gamma)^{20}\text{Ne}$, $^{20}\text{Ne}(\alpha, \gamma)^{24}\text{Mg}$, $^{13}\text{C}(\alpha, n)^{16}\text{O}$, and other (α, γ) , (α, n) and (α, p) reactions with the included isotopes) and C burning. The initial mixtures of elements and isotopes are prepared using the solar-system chemical composition of Asplund et al. (2009) that

is scaled to specified values of $[\text{Fe}/\text{H}]^3$. We assume that for $[\text{Fe}/\text{H}] \leq -0.7$ the initial mixtures are α -element enhanced with $[\alpha/\text{Fe}] = +0.4$. The appropriate Type 1 and Type 2 (with enhanced C and O abundances) OPAL and low-temperature molecular opacities have been prepared for such mixtures (Denissenkov et al. 2017b) and used in our computations.

The CO WD models are made with the inlists from the MESA test suite example `make_co_wd`. With these inlists the MESA code first computes the evolution of an intermediate-mass star from the pre-main sequence to the completion of the first He-shell thermal pulse on the AGB (blue curves in Figure 1, initial masses given in each panel), then the Blöcker AGB wind parameter (Blöcker 1995) is increased from 0.1 to 5 to mimic the enhanced mass loss caused by a common-envelope interaction in a close binary system in which the AGB star overflows its Roche lobe. As a result, the model star leaves the AGB and evolves towards and down the WD cooling track (green curves in the same Figure).

Our computations include convective boundary mixing (CBM) adopting the exponentially decaying diffusion model (Herwig et al. 1997):

$$D(r) = D_0 \exp\left(\frac{-2|r - r_0|}{f H_P}\right), \quad (1)$$

where D_0 is a value of the convective diffusion coefficient provided by the mixing-length theory (MLT) and H_P is the pressure scale height, both evaluated at $r = r_0$ in the vicinity of the respective convective boundary. For the boundaries of the H and He convective cores we have adopted the value of $f = 0.014$ that is close to the one constrained by the position of the terminal-age main sequence (TAMS) in a large number of stellar clusters (Herwig 2000). For the top and bottom boundaries of the He-flash convective zone we use the values of $f_{\text{top}} = 0.1$ and $f_{\text{bot}} = 0.008$ that are equal or close to those obtained in the multi-dimensional hydrodynamic simulations of the He-shell flash convection by Herwig et al. (2007). The value for f_{bot} is consistent with a number of abundance observables of *s*-process elements and H-deficient stars (Herwig 2005; Werner & Herwig 2006; Battino et al. 2016). Our stellar models evolve through the phases of convective H and He core burning and on the RAWD phase they experience convective He shell burning, therefore the above constraints for the values of f can be applied to them. We provide further support from new hydrodynamic simulations for our choice of f_{top} in §3.

When the CO WD model cools down to $\log_{10} L/L_{\odot} = -2$, we initiate a slow accretion of H-rich matter on it with $\dot{M}_{\text{acc}} \approx 10^{-8} M_{\odot} \text{ yr}^{-1}$ using the MESA mass-change control parameter in a new inlist with the same as before input physics. A higher value of \dot{M}_{acc} at this stage would result in MESA iterations having not converged. We assume that the accreted matter has the initial chemical composition of the binary. Because the accretion rate is now lower than the one required for stable H burning, our model exhibits mild H-shell flashes, each of them being followed by the expansion of its envelope. To stop the model from becoming

³ $[A/B] = \log_{10}(N(A)/N(B)) - \log_{10}(N_{\odot}(A)/N_{\odot}(B))$, where $N(A)$ and $N(B)$ are the abundances (number densities or mass fractions) of the nuclides A and B.

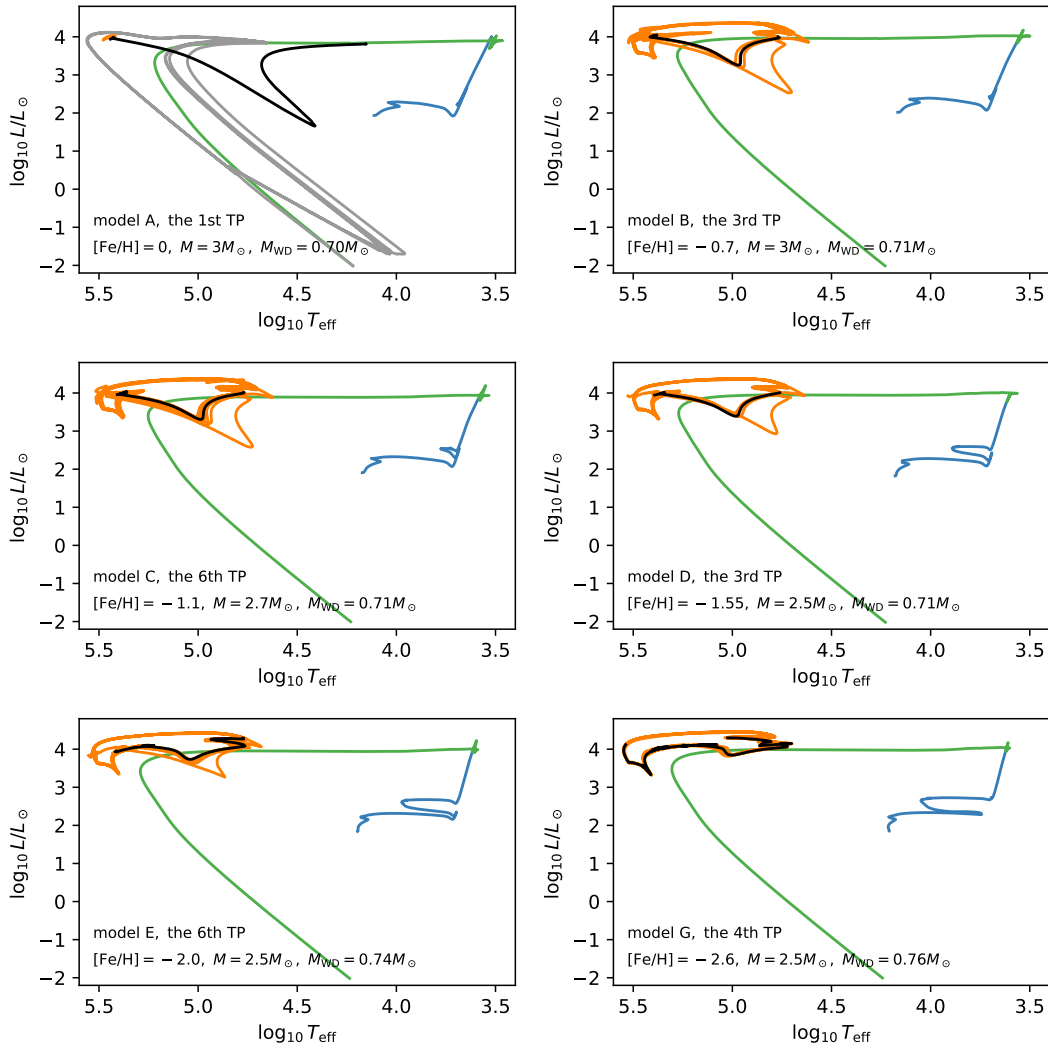


Figure 1. The evolutionary tracks of the progenitors of our RAWD models (blue and green, the pre-MS phase is not shown) and the tracks of the multicycle RAWD evolution (orange; the evolution goes counterclockwise in the cycles). The grey curve in model A panel shows the nova-like evolutionary loops that are used to reach the starting point, at the high- T_{eff} and high- L knee of the nova loop, of the RAWD evolution modelling. Text in the panels indicates the models and the serial numbers of their He-shell thermal pulses (TP) that are chosen for the post-processing simulations of the i-process nucleosynthesis, the black curves showing their tracks. The other parameters of these models are listed in Table 1. Model F is not shown here because its track and i-process yields are very similar to those of model G that we use to reproduce the surface abundances of heavy elements in CEMP-r/s stars.

a red giant, we enforce a mass loss by implementing the MESA super-Eddington wind prescription with an artificially reduced value of L_{Edd} , so that the model returns to the accretion phase and continues to make nova-like loops on the Hertzsprung-Russell diagram (a grey curve in the top-left panel of Figure 1; it is shown only for the progenitor of the solar-metallicity RAWD model A). During the stable H burning at a higher accretion rate a RAWD remains near the high- T_{eff} and high- L “knee” of a nova loop (e.g. Wolf et al. 2013), therefore we switch the accretion rate to a higher value in a model that is located near the knee. We adjust a value for \dot{M}_{acc} that would guarantee stable H burning and allow relatively large time steps between consecutive evolutionary models.

The RAWDs spend most of their time stably burning

the accreted H at the knees of nova loops, during which they should be seen as super-soft X-ray sources, unless being obscured by the ejected circum-binary matter (van den Heuvel et al. 1992; Lepo & van Kerkwijk 2013; Woods & Gilfanov 2016). Just as in thermal-pulse AGB stars, when a critical mass of He is accreted from the H-burning shell, a He-shell flash occurs causing an expansion of the accreted envelope (Figures 2a and 2f). Whereas the mass loss via the radiation-driven super-Eddington wind becomes less efficient at sub-solar metallicities, a fast and efficient mass loss can still be assumed for a star in a close binary system when it expands and overflows its Roche lobe. Therefore, a slightly modified MESA scheme for the Roche-lobe wind has been implemented in the present work to model the mass loss by our RAWD models during their expansion driven by the He-shell flashes.

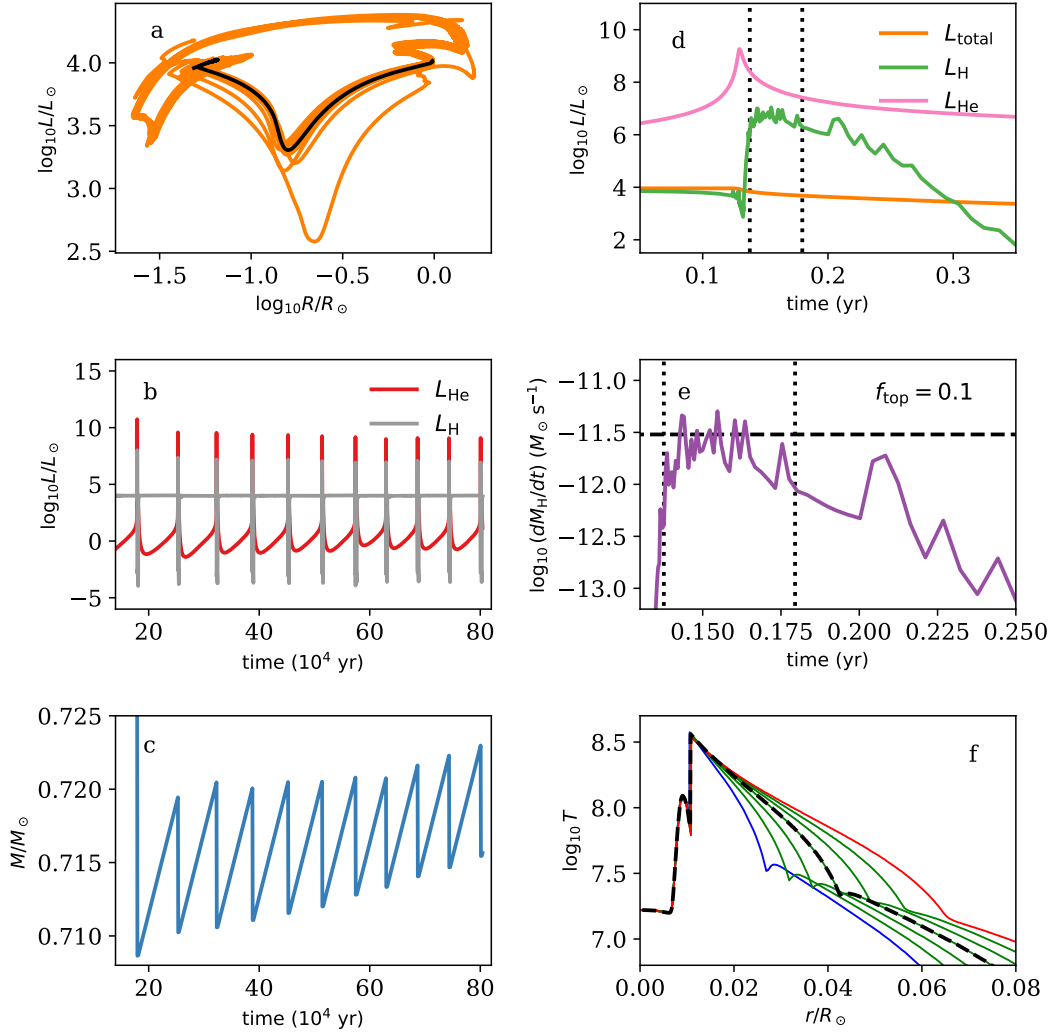


Figure 2. The evolution of luminosities, total mass, H-ingestion rate and temperature profile for the RAWD model C from the middle-left panel of Figure 1. Panel a shows the changes of the total luminosity with the radius during eleven consecutive He shell flashes (the evolution goes counterclockwise in the cycles) for which the corresponding changes of the H and He luminosities are shown in panel b and the changes of the total mass in panel c. The expansion of the RAWD is bounded by its assumed $2 M_{\odot}$ Roche-lobe radius (Equation 2). Panels d and e show how the luminosities and H-ingestion rate change with time during the 6th He shell flash (the black line segment in panel a). The wiggles on the L_H and \dot{M}_H curves are caused by the fact that the CBM prescription (1) is non-local and therefore its implementation in MESA is decoupled from the solution of stellar structure equations. Panel f: the evolution of the temperature profile in the RAWD during the 6th He shell flash. The black dashed curve was used in the post-processing computations of nucleosynthesis in the He convective zone.

While the MESA code approximates the Roche-lobe mass-loss rate as

$$\dot{M}_{\text{RL}} = \dot{M}_{\text{RL},0} \exp\left(\frac{R - R_{\text{RL}}}{H_{\text{RL}}}\right),$$

where $\dot{M}_{\text{RL},0}$ is a base value for which we use $10^{-3} M_{\odot} \text{ yr}^{-1}$, R_{RL} is the Roche-lobe radius of the mass-losing star, and H_{RL} is the Roche-lobe wind scale height, we prefer to use the following prescription:

$$\dot{M}_{\text{RL}} = \dot{M}_{\text{RL},0} \left(\frac{R}{R_{\text{RL}}}\right)^6 \quad (2)$$

for $R > 0.2 R_{\text{RL}}$. The implementation of our prescription for the Roche-lobe mass loss, that is equivalent to the MESA ap-

proximation for $|R - R_{\text{RL}}| \ll R_{\text{RL}}$ if one uses $H_{\text{RL}} = R_{\text{RL}}/6$, results in a smoother evolution of the RAWD models. After having lost a certain amount of mass with the Roche-lobe wind, which determines the mass retention efficiency, our RAWD model returns to the knee, and the H mass accretion resumes.

2.2 The RAWD i-process nucleosynthesis

The i process in an RAWD commences when the top of the He convective zone reaches the bottom of its H-rich surface layer, soon after the He-shell flash peak luminosity. At this moment, the He-shell convection begins to ingest protons (the left dotted line in Figure 2d marks the moment when

the H luminosity suddenly increases by more than two orders of magnitude as a result of the beginning H ingestion). It should be noted that our MESA computations find such H ingestion in all of our RAWD models even when $f_{\text{top}} = 0$ (Paper I), i.e. even when convective boundary mixing at the top boundary of the He convective zone is not included (although the H ingestion rate \dot{M}_H does positively correlate with f_{top}).

The i process in our RAWD models is simulated in post-processing computations similar to those carried out to model the i-process nucleosynthesis in Sakurai's object (Herwig et al. 2011; Denissenkov et al. 2018). These computations use the NuGrid multi-zone post-processing nucleosynthesis parallel code mppnp (Pignatari et al. 2016) customized for the H-ingestion He-shell problem. The input data for this code include a static or time-dependent structure of the He convective zone (this work uses the first option), i.e. the radius r , temperature T , density ρ , and convective diffusion coefficient D_{conv} at each point of its mass mesh, the chemical compositions of the He zone and of the ingested matter, the mass ingestion rate \dot{M}_{ing} and its duration t_{ing} .

Whereas the ingested matter has the initial chemical composition of the binary, the composition of the He convective zone at the beginning of H ingestion is obtained by processing the initial mixture through complete H burning followed by its processing via partial He burning, until the increasing C abundance matches its value from the corresponding MESA RAWD model, for which we use the NuGrid single-zone code ppn (cf. Denissenkov et al. 2018).

Our i-process nucleosynthesis simulations include ~ 1000 isotopes and ~ 15000 reactions. The reaction rates for these simulations are taken from the same list of references as in Denissenkov et al. (2018). We adopt an equally spaced 100-zone mass grid for the He shell region by interpolating the stellar structure variables to the new mesh. At each time step Δt , we add $X_o^k \dot{M}_{\text{ing}} \Delta t$ mass of the k th isotope from the envelope to the top $\Delta M = 1 - 4 \times 10^{-4} M_{\odot}$ of the He shell that occupies ~ 10 mass zones, as described in Appendix A.

2.3 The mass ingestion rate and duration

The mass ingestion rate \dot{M}_{ing} is determined from a combination of constraints from three-dimensional simulations (see §3) and the MESA RAWD stellar evolution simulations. Given the modelling choices described in the previous section the 1D stellar evolution simulations predict the ingestion of H-rich envelope material into the He-shell flash convection zone as it expands outward in Lagrangian coordinate. The protons ingested into the convection zone lead to a H-burning luminosity L_H which reflects the mass ingestion rate through the relation $\dot{M}_H = X_{\text{surf}} \dot{M}_{\text{ing}}$, where X_{surf} is the H mass fraction at the RAWD surface, and

$$\dot{M}_H \approx \frac{L_H}{\varepsilon_H}, \quad (3)$$

where ε_H is the energy released per one gram of burned H.

Because only the first two reactions of the CNO cycle are fast enough to occur in the He-shell convective zone during a convective overturn time, we assume that $\varepsilon_H = 0.667 \varepsilon_{\text{CNO}}$, where $\varepsilon_{\text{CNO}} \approx 6.3 \times 10^{18} \text{ erg g}^{-1}$ is the energy released per one gram of H transformed into He in

the full CNO cycle, and the factor 0.667 is the fraction of this energy produced per one gram of consumed H in the reactions $^{12}\text{C}(p, \gamma)^{13}\text{N}$ and $^{13}\text{N}(e^+ \nu)^{13}\text{C}$.

For the duration of mass ingestion t_{ing} , we adopt the values estimated from our MESA RAWD models. We use $\dot{M}_H(t)$ curves, like the one shown in Figure 2e, to estimate a time interval t_{ing} during which \dot{M}_H remains close to its maximum value wiggling around some nearly constant mean value, the latter giving us an estimate of \dot{M}_H . We check that the estimated values of t_{ing} do not exceed their upper limits constrained by the condition $t_{\text{ing}} < M_{\text{env}}/\dot{M}_{\text{ing}}$. The adopted values of \dot{M}_{ing} and t_{ing} used in the different simulations are summarized in Table 1. Although this is a somewhat subjective method of choosing the \dot{M}_{ing} and t_{ing} input data for the post-processing nucleosynthesis simulations, we think its accuracy is consistent with our using a static temperature profile, like the black dashed curve in Figure 2f, in these simulations.

3 INGESTION RATES AND CONVECTIVE BOUNDARY MIXING PARAMETERS FROM 3D HYDRODYNAMIC SIMULATIONS

The ingestion of material from the stable layer into the convection zone is the result of complex mixing processes at the convective boundary that may involve global, large-scale flow modes revealed in full 4π three-dimensional hydrodynamic simulations (Woodward et al. 2015). As mentioned in §2.1 we adopt in one-dimensional simulations the exponentially decaying CBM model with an efficiency parameter f_{top} to describe this mixing.

Both the mass ingestion rate and the convective boundary parameter f_{top} can be determined from hydrodynamic simulations, as demonstrated by Jones et al. (2017). For this purpose we have performed 3D hydrodynamic simulations of the He-shell flash convection zone and H ingestion in a RAWD using the PPMSTAR code (Woodward et al. 2015). It is an explicit Cartesian-grid-based code for 3D hydrodynamics built around the Piecewise-Parabolic Method (PPM; Woodward & Colella 1981, 1984; Colella & Woodward 1984; Woodward 1986, 2007). The code advects the fractional volume of the lighter fluid in a two-fluid scheme using the Piecewise-Parabolic Boltzmann method (PPB; Woodward 1986; Woodward et al. 2015). Thanks to PPB's use of subcell information, it needs two to three times fewer grid cells along all three axes than PPM to reach the same level of fidelity in the advection of a quantity, like the multifluid mixing fraction, whose value is conserved along stream lines. The code was designed with strong emphasis on parallel efficiency and it has performed past simulations of shell convection on up to 440,000 CPU cores on the NCSA Blue Waters computer (Woodward et al. 2015; Herwig et al. 2014).

The radial stratification of simulations is based on model A from Paper I. Like model A in the present paper, model A in Paper I had the solar initial chemical composition, but it had a bit lower mass of $0.65 M_{\odot}$. We consider the point in time 7.44hr after the beginning of the second He-shell flash in that model, when its He luminosity has dropped to $4.10 \times 10^9 L_{\odot}$ from its maximum value of $7.4 \times 10^{10} L_{\odot}$, and H ingestion into the He shell has just started.

The initial stratification of the 3D simulations follows

Table 1. Summary of the one-dimensional RAWD simulation parameters ($L_{\text{He}}^{\text{ing}}$ is the He luminosity at the beginning of H ingestion).

model	[Fe/H]	$M_{\text{WD}} (M_{\odot})$	$\dot{M}_{\text{acc}} (M_{\odot} \text{ yr}^{-1})$	$\log_{10}(L_{\text{He}}^{\text{max}}/L_{\odot})$	$\log_{10}(L_{\text{He}}^{\text{ing}}/L_{\odot})$	$\dot{M}_{\text{ing}} (M_{\odot} \text{ s}^{-1})$	$t_{\text{ing}} (\text{yr})$	$\eta (\%)$
A	0.0	0.70	2.6×10^{-7}	10.9	9.1	$2.2(35) \times 10^{-12}$	0.17(0.024)	–
B	−0.7	0.71	1.7×10^{-7}	9.5	8.5	2.0×10^{-12}	0.054	4.9
C	−1.1	0.71	1.5×10^{-7}	9.3	8.4	4.0×10^{-12}	0.042	4.9
D	−1.55	0.71	1.5×10^{-7}	9.3	8.5	4.2×10^{-12}	0.083	9.6
E	−2.0	0.74	1.7×10^{-7}	8.7	8.1	3.3×10^{-12}	0.060	27
F	−2.3	0.75	1.5×10^{-7}	9.2	8.6	2.4×10^{-11}	0.058	19
G	−2.6	0.75	1.5×10^{-7}	8.5	8.0	6.7×10^{-12}	0.087	29

the same approach as in Woodward et al. (2015) and approximates the 1D model with three polytropes: a lower stable layer (radial range $6 \text{ Mm} < r < 7.4 \text{ Mm}$), a convection zone ($7.4 \text{ Mm} < r < 33.5 \text{ Mm}$), and an upper stable layer ($33.5 \text{ Mm} < r < 50.0 \text{ Mm}$). We neglect radiation pressure, which contributes less than 25% to the total pressure in the 1D model, and we use the equation of state for a monoatomic ideal gas. To obtain a similar overall stratification with the slightly different equation of state, we use a small mean molecular weight $\mu_1 = 0.3$ for the fluid \mathcal{F}_1 initially filling the upper stable layer. The rest of the simulation domain contains fluid \mathcal{F}_2 with $\mu_2 = 1.4$. The two fluids are allowed to react with each other via the $^{12}\text{C}(p, \gamma)^{13}\text{N}$ reaction, assuming that \mathcal{F}_1 contains 88.6% of protons and \mathcal{F}_2 contains 20.4% of ^{12}C by number. The subsequent decay of ^{13}N is not considered. Convection in the He shell is driven by volume heating applied between the radii 7.9 Mm and 8.9 Mm.

The 3D simulations are done in 4π geometry on a Cartesian grid. We measure the luminosity dependence of the mass ingestion rate using runs E8, E13, and E15 (see Table 2), which cover a range of 1.4 dex in the driving luminosity L_{He} at the grid resolution of 768^3 , and one high-resolution run E10 (1536^3) with the same driving luminosity as its 768^3 equivalent E8.

Hydrogen ingestion starts as soon as the first upwelling plumes reach the upper convective boundary. After a few convective overturns a balance between hydrogen ingestion and burning is reached and the convective-reactive flow becomes quasi-stationary. We do not find a GOSH in these H-ingestion simulations which differs from the results found in the case of Sakurai’s object (Herwig et al. 2014). This corresponds to the result from 1D stellar evolution reported in Paper I and also found in most simulations here that the H ingestion does not cause a split of the convection zone, with the exception of model A where a split happens in very late phases (see §4).

Figure 3 shows that the ingestion process is dominated by large scales. The average hydrogen luminosity L_{H} reaches 2–3% of the driving luminosity L_{He} (Table 2). Ingestion events localised in time and space can have a much stronger influence on the flow than these small values suggest, but they are not strong enough to launch a global ingestion instability such as the GOSH phenomenon observed by Herwig et al. (2014) in their 3D simulations of Sakurai’s object.

The amount of mass $\dot{M}_{\text{ing}}(t)$ ingested into the convection zone by a time t is the sum of mass $\dot{M}_{\text{p}}(t)$ present in the convection zone at this time and mass $\dot{M}_{\text{b}}(t)$ burnt in the convection zone by this time. The radius r_{ub} of the up-

per boundary of the convection zone increases in time as a result of both mass ingestion and thermal expansion. We define r_{ub} to be the radius at which the radial gradient of the root-mean-square horizontal velocity $v_{\text{h}}(r)$ reaches a local maximum and we integrate the density of the ingested fluid up to the radius $r_{\text{top}} = r_{\text{ub}} - H_{v, \text{ub}}$, where the velocity scale height $H_{v, \text{ub}} = (\partial v_{\text{h}} / \partial r)^{-1}$ is evaluated at r_{ub} . The subtraction of $H_{v, \text{ub}}$ mitigates issues related to the large contrast in the concentration of the ingested fluid between the boundary region and the bulk of the convection zone (for details, see Jones et al. 2017). To find the burnt mass $\dot{M}_{\text{b}}(t)$, we compute the mass burning rate from spherically-averaged profiles of temperature, density, and fractional volume of ingested fluid at regularly-spaced points in time; $\dot{M}_{\text{b}}(t)$ is then obtained by time integration. The resulting time dependence of \dot{M}_{p} , \dot{M}_{b} , and \dot{M}_{ing} in run E10 is shown in Fig. 4. We obtain the ingestion rate \dot{M}_{ing} by fitting a straight line to $\dot{M}_{\text{ing}}(t)$.

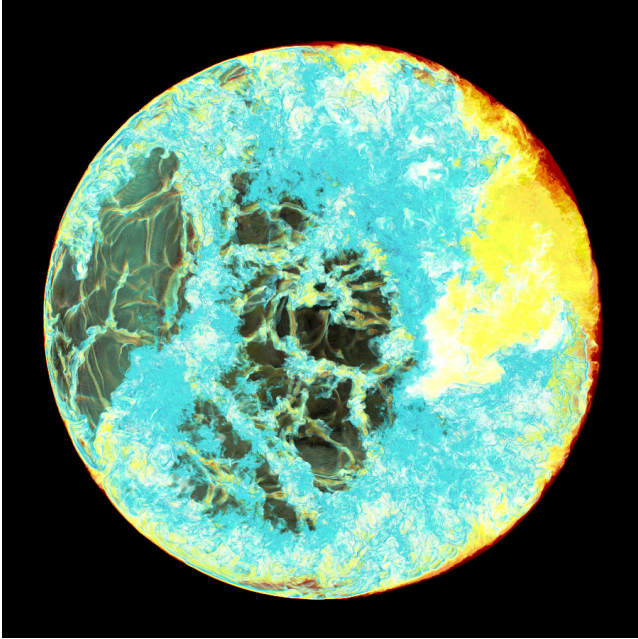
Figure 5 shows that the ingestion rate scales in proportion to the driving luminosity L_{He} , in agreement with the results of Jones et al. (2017) on the O-shell convection in massive stars. This is likely to be caused by the fact that the ingestion rate is limited by the amount of work needed to be done to overcome the buoyancy of the ingested material, as argued by Spruit (2015). The ingestion rate in run E8 (768^3) is only 26% lower than in run E10 (1536^3) of the same luminosity, which provides an idea of the resolution dependence of these entrainment rate results.

The ingestion rates measured in 1D models B–F are close to the scaling relation established by the 3D hydrodynamic simulations, which may not have been expected given the numerous differences between the 1D and 3D models. For the RAWD models in Figure 5, we have used the He-shell luminosity at the moment when the top of the He convective zone reaches the bottom of the H-rich envelope and, as a result of this, the H-burning luminosity quickly increases. These luminosities are somewhat lower than their corresponding peak He luminosities (e.g., panel d in Figure 2). In any case, the ingestion rates adopted for our nucleosynthesis simulations are consistent with the results obtained with the 3D hydrodynamic simulation in the sense that they are close to the scaling relation between the driving luminosity of the convection and the ingestion rate established by three 768 -grid hydrodynamic simulations.

We can also obtain information on the convective boundary mixing efficiency at the top of the He-shell flash convection zone. As in Jones et al. (2017) we determine the f parameter from the evolution of the spherically averaged radial profiles of the abundance of the H-rich fluid that is entrained into the He-shell flash convection zone (Figure 6).

Table 2. Summary of our 3D PPMSTAR simulations.

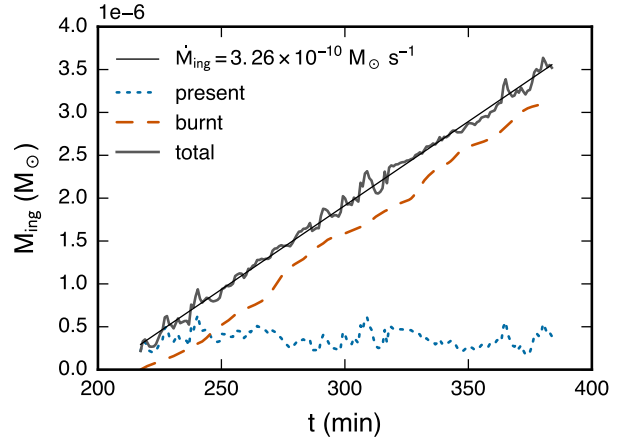
run	grid	$\log_{10} L_{\text{He}}/L_{\odot}$	$L_{\text{H}}/L_{\text{He}}$	$\dot{M}_{\text{ing}} (M_{\odot} \text{ s}^{-1})$
E8	768 ³	9.95	0.025	2.32×10^{-10}
E10	1536 ³	9.95	0.034	3.26×10^{-10}
E13	768 ³	10.65	0.019	9.45×10^{-10}
E15	768 ³	11.35	0.020	5.04×10^{-9}

**Figure 3.** Fractional volume (FV) of the fluid ingested into the convection zone in run E10 at $t = 359.8$ min. The colour scheme is such that the lowest values of FV are transparent, then when FV increases the colour changes from blue through white and yellow to red. Finally, the black colour corresponds to $\text{FV} = 1$, so that the stable layer is not seen. The front half of the sphere is not shown and the camera is looking into the back half of the sphere in this rendering.

This is done by solving the inverted Lagrangian diffusion equation which gives the diffusion coefficient profile that would have been needed to advance from an abundance profile at a time t to a profile at time $t + \Delta t$ by means of a 1D diffusion process. The time difference Δt is usually taken to be one or a few convective overturning time scales. The details of this procedure have been improved somewhat over the approach in Jones et al. (2017) and will be described elsewhere in detail. For the high-resolution E10 simulation we determine $f_{\text{top}} = 0.434$.

This value is larger than the one appropriate for our 1D simulations because the E10 hydrodynamic simulation has been performed at a driving luminosity that is 141 times higher than, for example, the He-burning luminosity in the stellar evolution run C ($\log L_{\text{He}} = 7.8$). In order to scale the f value obtained in our higher-luminosity hydro simulation to the actual lower luminosity of the stellar evolution RAWD model we use the scaling relationship

$$f_{\text{top}} \propto L_{\text{drive}}^{1/3} \quad (4)$$

**Figure 4.** Time dependence of the amounts of ingested fluid present and burnt in the convection zone in run E10. The rate of change of their total mass is the ingestion rate \dot{M}_{ing} . The amount of fluid burnt is counted from zero at the beginning of the shown time series.

between the driving luminosity of a shell convection and the convective boundary mixing parameter f_{top} at the top of the convection zone. This relationship has been derived from a series of new 1536-grid 3D hydrodynamic simulations of O-shell convection as in Jones et al. (2017), but with an improved version of the PPMSTAR code (Figure 7). These simulations, the f determination and the resulting scaling law will be described in detail elsewhere. However, this relationship can be motivated within a simplistic picture in which the CBM f parameter is a measure of how much convective plumes can deform the convective boundary and penetrated into it before being decelerated by their negative buoyancy upon entering the stably stratified regions. It would be the momentum of the convective plume that determines the level of penetration and boundary deformation. The convective velocity scales with one third power with the luminosity (Biermann 1932; Porter & Woodward 2000; Müller & Janka 2015; Jones et al. 2017). The scaling relation Eq. (4) reflects this reasoning: $f \propto v \propto L^{1/3}$.

Applying relation Eq. (4) to scale $f_{\text{top}} = 0.434$ from the E10 driving luminosity of $\log L_{\text{He}} = 9.95$ to the driving luminosity of the stellar evolution model C at the time of H ingestion ($\log L_{\text{He}} = 7.8$) we obtain $f_{\text{top}} = 0.08$. This provides strong support for the value $f_{\text{top}} = 0.10$ that we have adopted in the RAWD stellar evolution simulation which are all at a similar He-burning luminosity at the time of ingestion.

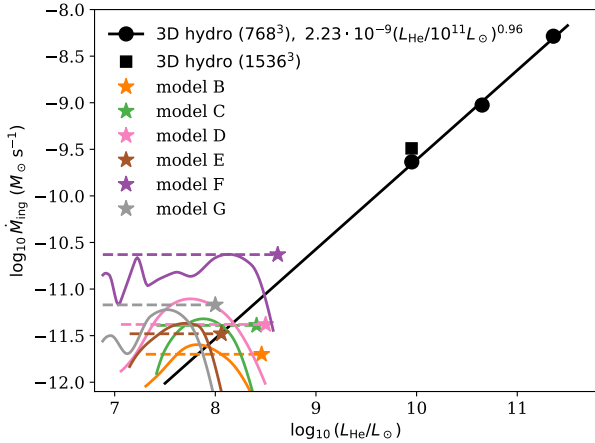


Figure 5. Ingestion rates as functions of He-burning luminosity that is driving convection according to the RAWD stellar evolution models and 3D hydrodynamic simulations. The black line is the L_{He} -scaling relation for the mass ingestion rate from the 3D hydrodynamic simulations that used the RAWD model A from Paper I for the initial setup. The filled black circles are the results of the individual $(768)^3$ hydro simulations and the filled black square is the result of the $(1536)^3$ hydro run (Table 2). The star symbols with adjacent horizontal dashed line segments are the average mass ingestion rates estimated for our 1D RAWD models as described in Section 4.2, while the arc curves of the same colours show smooth fits to the actual variations of \dot{M}_{ing} with L_{He} in these models. The star symbols are located at $L_{\text{He}} = L_{\text{He}}^{\text{ing}}$ that corresponds to the beginning of H ingestions in 1D models (Table 1)

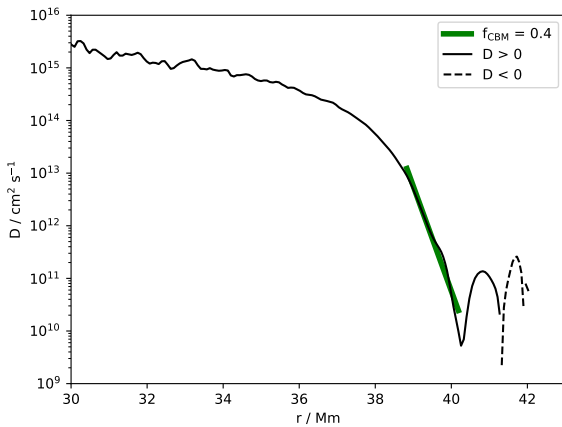


Figure 6. Determination of the f_{top} mixing parameter from the high-grid-resolution 3D hydrodynamics simulation E10.

4 RESULTS

4.1 The RAWD multicycle evolution

Using the methods described in Section 2.1, we have computed the evolution of seven RAWD models with the metallicities and WD masses listed in Table 1 along with other model parameters. The evolutionary tracks of six of these

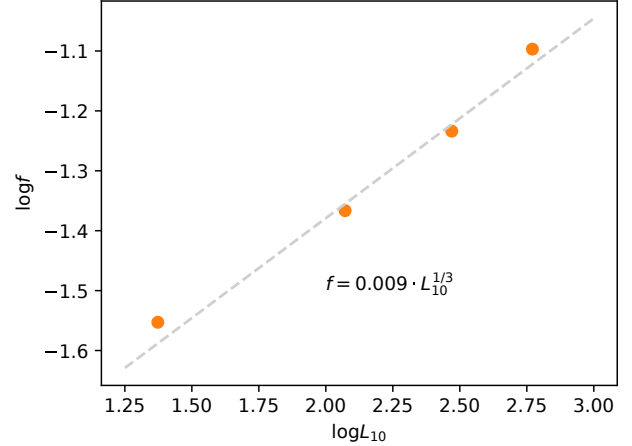


Figure 7. Scaling relation of the convective boundary mixing parameter f_{top} versus the driving luminosity based on a series of 1536-grid simulations of O-shell convection with the same setup as in Jones et al. (2017).

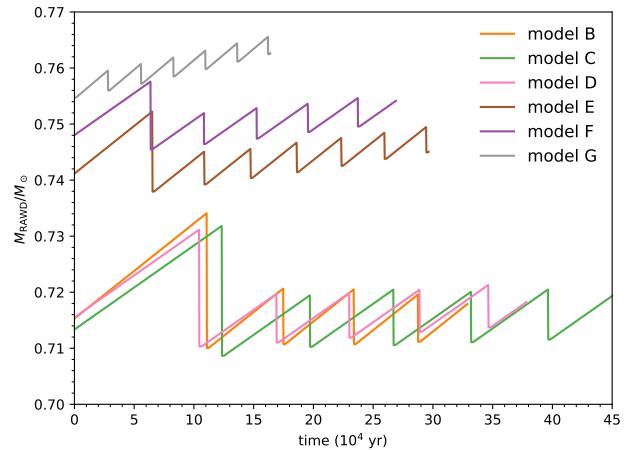


Figure 8. The changes of the total mass of our RAWD models caused by the accretion and Roche-lobe mass loss.

models are shown in Figure 1, where their initial masses are also indicated. Except the solar-metallicity model A, we have simulated the RAWD evolution for many cycles, typically more than five, (orange curves in Figure 1). The multicycle evolution of the solar-metallicity RAWD models was discussed in Paper I. Black curve segments in Figure 1 highlight the relatively short-lasting evolutionary phase of the He-shell thermal pulse (TP) whose serial number is specified for each model and that has been chosen for the *i*-process post-processing nucleosynthesis computations in Section 4.2.

All of the RAWD models have nearly the same initial central temperature with $\log_{10} T_c \approx 7.2$ and use the same WD Roche-lobe radius $R_{\text{RL,WD}} = 2R_{\odot}$ in Equation 2 that corresponds to the orbital period $P \approx 1.2$ days for a secondary mass of $\sim 2M_{\odot}$.

The new computations of the RAWD multicycle evolution confirm the conclusion about their low mass retention

efficiency (the last column of Table 1 and Figure 8) made in Paper I, at least for $[\text{Fe}/\text{H}] \gtrsim -2$. A new result is that η increases when $[\text{Fe}/\text{H}]$ decreases below -2 to fractions of ≈ 20 to 30% in models E, F and G. The $0.75M_{\odot}$ RAWD model with $[\text{Fe}/\text{H}] = -2.6$ (model G) has the highest value of $\eta = 29\%$ and a lower He peak luminosity of $\log_{10} L_{\text{He}}^{\text{max}} = 8.5$ (the last row in Table 1) compared to models E and F. According to these models the SD channel of SNIa progenitors may still work at very low metallicities.

The revealed trend of η with $[\text{Fe}/\text{H}]$ is probably caused by the lower opacity of the metal-poor accreted matter. It allows the accumulated He layer to cool down, and therefore be compressed by the gravity more efficiently. As a result, the He flash starts at a lower mass of the He shell and achieves a lower peak luminosity, which is reflected in the different amplitudes of the RAWD mass changes in the models with $[\text{Fe}/\text{H}] < -1.55$ (E and F) compared to the models with $[\text{Fe}/\text{H}] \geq -1.55$ (B, C and D) in Figure 8, and in their different values of $\log_{10} L_{\text{He}}^{\text{max}}/L_{\odot}$ (Table 1). Besides, during the expansion of the RAWD following the He-shell flash its envelope cools down faster, because of the lower opacity, in the low-metallicity models, and the RAWD returns to the accretion phase after having lost a smaller fraction of the accreted matter.

As for the RAWD models with $[\text{Fe}/\text{H}] \geq -1.55$, they stubbornly want to expand to red-giant dimensions and it is only because of our implementation of the Roche-lobe mass loss that they can expand only up to $R \approx R_{\text{RL,WD}}$ (Figure 2a) and retain this radius until a significant fraction of the accreted matter is gone with the wind. To test if this behaviour is affected by our choice of the MESA mass-loss algorithm, we have switched to the super-Eddington wind prescription in model C, enforcing it to work only when $R \approx R_{\text{RL,WD}}$. With this modification, we have reproduced the results obtained for model C with the Roche-lobe mass-loss prescription.

We have also addressed the frequently raised concern that a much larger number of He-shell flashes than we have simulated in our RAWD models could lead to significant changes in the RAWD multicycle evolution. To test this, we have extended the computed number of the He-shell flashes in model C up to 42 from the initial 10. The results of this long-run simulations are plotted in Figure 9. Its top panel demonstrates that the WD central temperature has increased only by 6%. Our analysis of the RAWD mass variations presented in the middle panel shows that the mass retention efficiency has varied between 5.8% and 8.8% in this run, still remaining below 10%, as it was in the initial 10 cycles. Finally, the bottom panel reveals that the He peak luminosity has not changed at all.

4.2 The RAWD i-process nucleosynthesis yields

Before presenting the yields, we will summarize how we choose the input data for the RAWD i-process nucleosynthesis computations. For this purpose, we use model C (Figure 2), as an example. We begin with selecting a representative RAWD He-shell flash that does not stand out, therefore this cannot be the first He-shell flash that usually is stronger than the others. The only exception to this rule in the present paper is the solar-metallicity model A. We find it to be much more difficult to compute multiple cycles

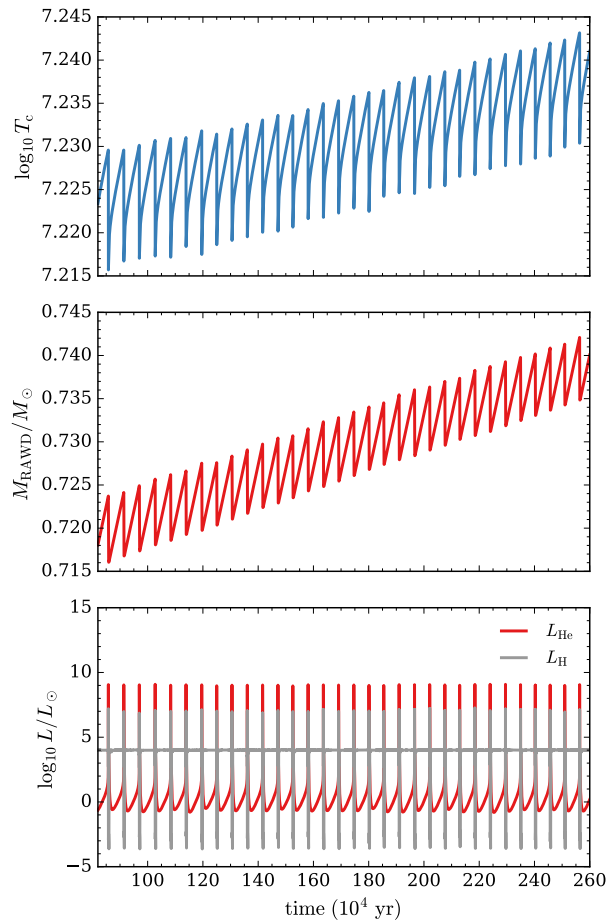


Figure 9. Central temperature, total RAWD mass and H- and He-burning luminosity as a function of time for the long-term multicycle evolution of model C.

with stable H burning interrupted by strong He-shell flashes at a high metallicity, probably because of the high opacity of the envelope matter. Because the multicycle evolution of the solar-metallicity RAWD models has already been discussed in Paper I, and the i-process yields calculated for the first He-shell flash in the solar-metallicity RAWD model in this work are similar to those presented in Paper I, we have followed only one He-shell flash in the new model A. As for model C, we have chosen the 6th flash (panels a, b and c in Figure 2). We have used its corresponding H-burning luminosity (panel d) to estimate the H-ingestion rate with Equation 3 (the purple curve in panel e). The dashed line in panel e is our estimate of an average \dot{M}_{H} value for this model that was used to calculate the parameter $\dot{M}_{\text{ing}} = (\dot{M}_{\text{H}}/X_{\text{surf}})$ listed in Table 1. The vertical dotted lines in panel e constrain t_{ing} . The left line is chosen close to the beginning of H ingestion. The position of the right line is less certain. It marks the beginning of the fast decline of \dot{M}_{H} . The H-ingestion time in the RAWD models is usually less than one month ($t_{\text{ing}} \lesssim 0.08$ yr), except the first phase of H-ingestion in model A. Like in the solar-metallicity model A from Paper I, the updated model A has two phases of H ingestion, the longer-lasting slow-ingestion phase with

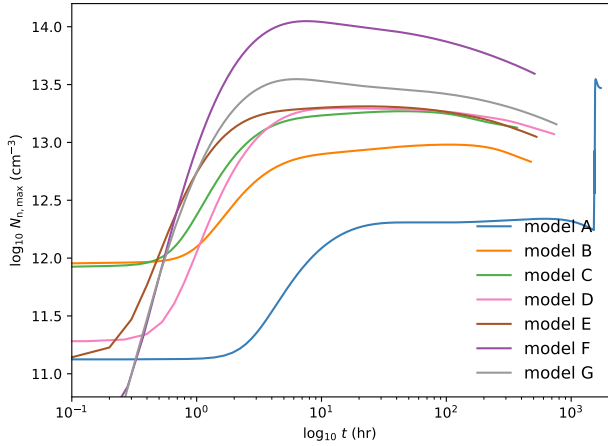


Figure 10. The evolution of the maximum neutron number density in the He convective zones of our RAWD models. In model A, the jump in the evolution of $N_{n,\max}$ at the end is caused by the switching to the second phase of H ingestion that is shorter but faster than the previous phase (see text).

$\dot{M}_{\text{ing}} = 2.2 \times 10^{-12} M_{\odot} \text{ s}^{-1}$ and $t_{\text{ing}} = 0.17 \text{ yr}$ followed by the shorter fast-ingestion phase with $\dot{M}_{\text{ing}} = 3.5 \times 10^{-11} M_{\odot} \text{ s}^{-1}$ and $t_{\text{ing}} = 0.024 \text{ yr}$, both included in our nucleosynthesis computations.

It usually takes about hundred time steps for the MESA code to evolve a RAWD model through the entire H-ingestion phase, meaning that the time interval between two consecutive models on this evolutionary phase is hundreds of minutes, corresponding to tens of convective turnover times of the He-shell flash convection. This is too long for the *i*-process nucleosynthesis simulations that usually require a time step of the order of minutes (Herwig et al. 2011). We cannot reduce the MESA time steps, because the mixing-length theory (MLT) adopted in MESA to describe convection is formulated in terms of time and spatial averages. Time steps smaller than about ten times the convective turnover time would violate this assumption. Therefore, we simply take the temperature, density, radius and MLT convective diffusion coefficient profiles from a MESA model in the middle of the H-ingestion phase, when the accreted envelope is already expanding (e.g., the dashed T profile in panel f), and use them to set up our post-processing nucleosynthesis simulations. Note, that Herwig et al. (2011) were able to reproduce the surface abundances of heavy elements measured in Sakurai’s object by Asplund et al. (1999) using a 1D model similar to this one.

The post-processing simulations of the *i*-process nucleosynthesis were carried out using the methods described in §2.2. The nucleosynthesis simulations provide the abundance distributions in the He convective zone and the surface abundances at the top of the He shell for the selected (~ 1000) isotopes for $0 \leq t \leq t_{\text{ing}}$. At the end, we allow the surface abundances to decay for 1 Gyr. Figure 10 shows the evolution of the maximum neutron number density in the He shell for our RAWD models. The peak value of the $N_{n,\max}(t)$ curves increases with a decrease of $[\text{Fe}/\text{H}]$ because the total mass fraction of the isotopes that capture neutrons decreases

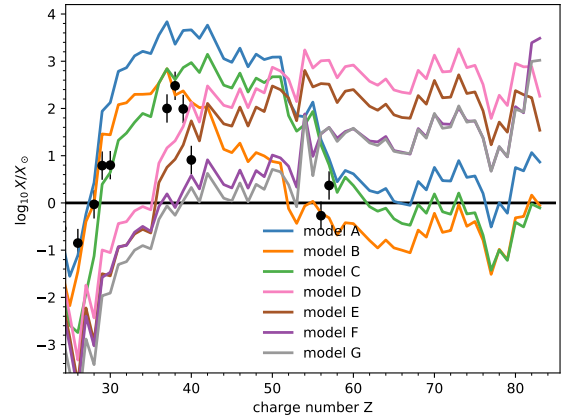


Figure 11. The elemental *i*-process yields (solar-scaled mass fractions) from our RAWD models. For comparison, the abundances of the first peak *n*-capture elements measured in Sakurai’s object by Asplund et al. (1999) are shown as filled black circles with errorbars. They were interpreted by Herwig et al. (2011) as results of the *i*-process nucleosynthesis in the convective He shell during its very last thermal pulse in a model of Sakurai’s object with a half-solar metallicity.

with the metallicity, while the production of neutrons, that is controlled by the ^{12}C abundance in the He shell and the total amount of ingested H, remains approximately the same. In other words, the neutron source is primary, while the *i*-process seeds are secondary. The steep increase of $N_{n,\max}$ at the end of its evolution in model A marks the beginning of the short fast-ingestion phase that appears to be common for solar-metallicity RAWDs (Paper I). It demonstrates that $N_{n,\max}$ increases with \dot{M}_{ing} for models with the same metallicity.

Figure 11 shows the final surface elemental abundances divided by the solar abundances from Asplund et al. (2009) of the RAWD models⁴. As in the *s* process the global heavy-element distribution shifts to higher mass elements at lower metallicity (Clayton 1968; Busso et al. 2001). We therefore, generally speaking, expect to see local elemental *i*-process signatures in higher-mass second- and third-peak species at lower metallicity, whereas the *i*-process signature may be most prominently detected in lower-mass, first-peak elements at higher, solar-like metallicities. Accordingly it had been proposed in Paper I that the solar-metallicity RAWDs could be contributors of first-peak elements to the solar system abundance distribution. Côté et al. (2018) have used our RAWD *i*-process yields in a framework that included Galactic chemical evolution and binary-star population synthesis models to confirm this hypothesis.

An example for solar-like metallicity *i*-process abundances are those of Sakurai’s object which indeed shows large enhancements in the first peak *n*-capture elements (around $Z = 40$) as shown in Figure 11. The details of the

⁴ The files with the elemental and isotopic abundance yields from our RAWD models can be found at <http://apps.canfar.net/storage/list/nugrid/data/projects/RAWD/iRAWDyields>

abundance patterns of Sakurai’s object are however better reproduced by the very-late thermal pulse post-AGB star models of [Herwig et al. \(2011\)](#) which feature peak neutron densities and H ingestion rates that are both more than two orders of magnitude higher compared to the RAWD models.

4.3 A possible relation of the metal-poor RAWDs to the CEMP-r/s stars

An example for i-process abundance patterns in the second-peak elements expected at lower metallicity may be found in the subclass of carbon-enhanced metal-poor (CEMP) stars with abundance patterns that appear to be enhanced with both *r*- and *s*-process elements (e.g. [Beers & Christlieb 2005](#); [Masseron et al. 2010](#); [Lugaro et al. 2012](#); [Bisterzo et al. 2012](#)). [Dardelet et al. \(2015\)](#) and [Hampel et al. \(2016\)](#) have done one-zone nucleosynthesis simulations of i-process conditions to demonstrate that the abundances of heavy elements observed in these CEMP-r/s stars can be reproduced by an n-capture process with neutron densities $N_n = 10^{12} - 10^{15} \text{ cm}^{-3}$.

As an example, Figure 12 shows the best χ^2 fit of the i-process elemental yields from our RAWD models G and F to the surface chemical composition of the CEMP-r/s star CS31062-050 that has the metallicity $[\text{Fe}/\text{H}] = -2.42$ ([Johnson & Bolte 2004](#)) intermediate between those assumed for our models F and G. The only exception to the otherwise excellent agreement is the discrepant Ba abundance that requires a further investigation. For other CEMP-r/s stars a good agreement with the RAWD i-process yields can be found as well, including their lower Ba abundances. The low-metallicity RAWD models are at this point the first and only models in which nucleosynthesis calculation directly post-processing complete stellar evolution models can reproduce the complete abundance patterns observed in CEMP-r/s stars. We therefore propose that CEMP-r/s stars that have been well reproduced with i-process models should be referred to as CEMP-i stars.

Our findings suggest a new scenario for the formation of CEMP-r/s, or in this case CEMP-i stars, that takes into account our finding that the RAWDs with $[\text{Fe}/\text{H}] \lesssim -2$ may reach the Chandrasekhar mass and explode as SNe Ia. It is based on the fact that the mass retention efficiency of our RAWD models significantly increases when $[\text{Fe}/\text{H}]$ decreases below -2 (the last column of Table 1), and it is supported by our calculations of the evolution of binary-star parameters. For these calculations, we have used the isotropic re-emission model of mass transfer in which a fraction β of matter accreted by the primary star (RAWD) is lost from the binary system. In our case, $\beta = 1 - \eta$, where η is the mass retention efficiency. This model and its equations are described by [Postnov & Yungelson \(2014\)](#) in their Section 3.3.3. We have solved these equations to model the evolution of the semi-major axis a , the mass ratio $q = M_1/M_2$, and the RAWD mass M_1 for two sets of the binary initial parameters. In both cases we start with $M_2 = 2.5 M_\odot$ and use $\dot{M}_2 = -1.5 \times 10^{-7} M_\odot \text{ yr}^{-1}$. The first case assumes that $\eta = 10\%$ which includes the RAWD models with $[\text{Fe}/\text{H}] \gtrsim -2$, while the second case has $\eta = 30\%$ and demonstrates a possible evolution of the binary-system parameters for RAWDs with $[\text{Fe}/\text{H}] \lesssim -2$. In both cases, we have stopped the calculations at $q = 2$.

In the first case, M_1 grows from $0.75 M_\odot$ to only $\sim 0.9 M_\odot$, while in the second case M_1 starts growing from $0.85 M_\odot$ and it does reach the Chandrasekhar limit, and the RAWD ends its life as a SNIa. If this is true, then some of the present-day CEMP-i stars could be former tertiary members of hierarchical triple systems in which they had been orbiting a close binary system with a RAWD. A series of dozens He-shell flashes on the RAWD, each being followed by the RAWD expansion and mass loss, could enrich the tertiary star with the products of i-process nucleosynthesis. This enrichment scenario is similar to the one proposed to explain abundance anomalies in CEMP-s stars by accretion of material lost by their AGB star binary companions (e.g., [Abate et al. 2018](#), and references therein). A difference is that tertiary stars in hierarchical triple systems are farther away from their polluting primary components. This should result in a stronger dilution of the accreted material. But, on the other hand, heavy elements produced in the s process in AGB stars are already diluted in their relatively massive envelopes before they are ejected, while the dilution in a thin envelope of an RAWD is negligible. If thermohaline mixing in envelopes of accreting stars leads to an even stronger dilution depends on the efficiency (timescale) of this mixing which still remains uncertain ([Denissenkov & Pinsonneault 2008](#); [Stancliffe et al. 2007](#)). For example, thermohaline mixing can be suppressed by strong horizontal turbulent diffusion ([Denissenkov 2010](#)). Finally, when the RAWD exploded as SNIa, the tertiary star, that became a CEMP-i star by that moment, would leave the triple system because of a decreased gravitational pull to the center of mass that has suddenly lost $\sim 1.4 M_\odot$. Those CEMP-i stars would not be binaries anymore. If the RAWD does not explode as a SN Ia the CEMP-i star would be possibly in a wider orbit around compact binary and would show a long binary period super imposed with the very short period of the compact RAWD binary. Thus, CEMP-i stars can be both single stars and binaries in this scenario. Our scenario is supported by the recent finding that the fractions of binary and triple star systems in stellar populations significantly increase with a decreasing metallicity ([Fuhrmann et al. 2017](#); [Badenes et al. 2018](#); [Moe et al. 2019](#)).

This scenario can potentially explain the observational bias against finding CEMP-r/s stars in globular clusters that may be caused by the destruction of wide triple systems through close star encounters in dense cores of globular clusters. Our scenario differs from the triple-system scenario for the formation of CEMP-r/s stars discussed by [Abate et al. \(2016\)](#), in which a primary massive star was assumed to produce the *r*-process elemental abundances during its SN explosion and the presence of a secondary AGB star was required to make *s*-process elements. The plausibility of our scenario could be checked with triple-star population synthesis simulations, but this is out of the scope of the present paper.

5 SUMMARY

We have used the MESA stellar evolution code ([Paxton et al. 2011, 2013](#)) to compute the models of CO white dwarfs (WDs) rapidly accreting H-rich matter, assuming this matter is donated by normal (main-sequence, sub-giant or red-

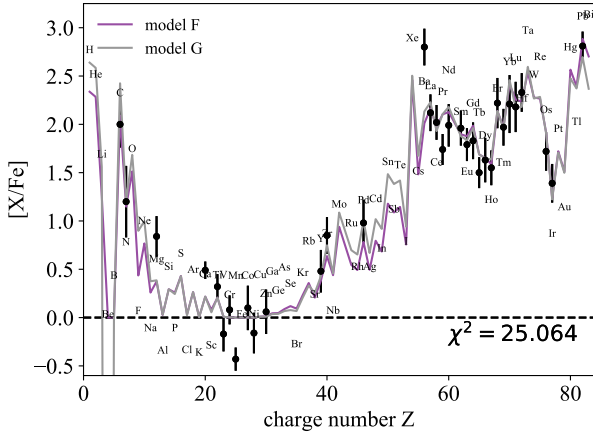


Figure 12. Abundances of heavy elements observed in the CEMP-r/s star CS31062-050 (Aoki et al. 2002; Johnson & Bolte 2004) and the best-fit abundance distribution from the time evolution of the RAWD model G, that has $[\text{Fe}/\text{H}] = -2.6$, diluted with 99.58% of the initial abundances. Most CEMP-r/s stars have metallicities in the range of $-3 \leq [\text{Fe}/\text{H}] \leq -2$ (e.g. Abate et al. 2016). A similarly good fit for the star CS31062-050 is obtained with the RAWD model F. The element names are placed either above or below (so that they do not overlap) the predicted abundances (curves).

giant-branch) components of the WDs in close binary systems. Such stellar configurations can result from common envelope events, after the primary AGB star components fill their Roche lobes, loose almost entire envelopes above the WD cores in unstable mass transfers, and the binary systems become tighter via the transformation of their orbital energies into the kinetic energy of the ejecta. When the secondary components of these post-common-envelope systems expand and fill their own Roche lobes by or after the end of the main-sequence evolution, they begin to donate H-rich matter to their, by this time cooled-down, WD primary components. We assume that the mass accretion rate is rapid enough, $\dot{M}_{\text{acc}} \sim 10^{-7} M_{\odot} \text{ yr}^{-1}$, for the accreted H to be stably burning on the WD surface, resulting in the accumulation of a He shell. When its mass reaches a critical value, the He shell will experience a thermal flash in which some fraction of He will be transformed into C. If the sequence of the stable H burning intermittent with the He-shell flashes is not accompanied by a significant mass loss by the WD, then its mass may eventually reach the Chandrasekhar limit, $M_{\text{Ch}} \approx 1.38 M_{\odot}$, and the CO WD will explode as a SNIa. This is the classical single degenerate (SD) channel of SNIa progenitors (Schatzman 1963; Whelan & Iben 1973).

In this work, the evolution of such rapidly-accreting WDs (RAWDs) has for the first time been followed through multiple strong He-shell flashes. Each He-shell flash leads to the expansion of the WD envelope that overflows the WD Roche lobe. We assume that the matter leaving the WD Roche lobe is lost from the binary system because of its interaction with the secondary component, like in the common-envelope event. The important new result found in our simulations is that the WD envelope remains inflated at the WD Roche-lobe radius until its significant fraction is

lost, after which it shrinks, and the mass accretion onto the WD resumes. As a result, we have obtained relatively low mass retention efficiencies, $\eta \lesssim 10\%$, for our RAWD models, at least for the metallicities $[\text{Fe}/\text{H}] \gtrsim -2$ (Table 1). It is unlikely that the masses of such RAWDs will ever approach the Chandrasekhar limit. Therefore, the SD channel should not work in these cases. As for the RAWD models with $[\text{Fe}/\text{H}] \lesssim -2$, they are found to have $\eta \gtrsim 20\%$ and, therefore, we cannot exclude that their masses will ultimately reach the Chandrasekhar limit.

The ignition of He at the bottom of the He shell triggers convection. When the top of the He-flash convective zone reaches the bottom of the H-rich envelope, convective boundary mixing (convective shear mixing and convective overshooting) starts to ingest protons into the He shell. There, they are quickly captured by the abundant ^{12}C nuclei producing the unstable ^{13}N that has the lifetime of ~ 10 minutes and decays into ^{13}C while being transported by convection downwards. When ^{13}C nuclei arrive at the bottom of the He shell they capture α particles releasing neutrons. This convective-reactive process transforms almost every proton ingested at the top of the He shell into a neutron at its bottom, therefore at sufficiently high mass ingestion rates, $\dot{M}_{\text{ing}} \sim 10^{-12} - 10^{-11} M_{\odot} \text{ s}^{-1}$, the neutron density can be as high as $N_{\text{n,max}} \sim 10^{12} - 10^{15} \text{ cm}^{-3}$. These values are intermediate between those characteristic of the *s* and *r* processes, therefore the ensuing n-capture process is called the *i*-process (Cowan & Rose 1977).

The important input parameters — the ingestion rate and convective boundary mixing efficiency — have been determined and constrained through a series of three-dimensional hydrodynamic simulations of the RAWD He-shell flash convection. The estimates of the mass ingestion rate obtained from 1D RAWD models are consistent with the 3D hydrodynamic simulations. The convective boundary mixing efficiency parameter adopted in our stellar evolution simulations at the top of the He-shell flash convection boundary are in agreement with the luminosity scaling law for the CBM f_{top} parameter presented here.

It is interesting that the *i*-process nucleosynthesis yields predicted by our metal-poor ($[\text{Fe}/\text{H}] \lesssim -2$) RAWD models almost perfectly fit the abundances of heavy elements measured in some CEMP-r/s stars (Figure 12). These are the CEMP-i stars. Given that the same RAWD models have the higher mass retention efficiencies and can potentially become SNeIa, we propose that CEMP-i stars used to be distant members of triple star systems orbiting close binary systems with RAWDs. When the RAWD exploded as a SNIa, the tertiary star, polluted by the products of *i*-process nucleosynthesis that had taken place on the RAWD, got loose from the system and is now seen as a single star. If the RAWD has not exploded yet, the CEMP-i star can still be a member of a triple system, and would then show signs of binarity.

ACKNOWLEDGEMENTS

FH acknowledges funding from NSERC through a Discovery Grant. This research is supported by the National Science Foundation (USA) under Grant No. PHY-1430152 (JINA Center for the Evolution of the Elements).

REFERENCES

- Abate C., Stancliffe R. J., Liu Z.-W., 2016, *A&A*, **587**, A50
- Abate C., Pols O. R., Stancliffe R. J., 2018, *A&A*, **620**, A63
- Aoki W., Norris J. E., Ryan S. G., Beers T. C., Ando H., 2002, *PASJ*, **54**, 933
- Asplund M., Lambert D. L., Kipper T., Pollacco D., Shetrone M. D., 1999, *A&A*, **343**, 507
- Asplund M., Grevesse N., Sauval A. J., Scott P., 2009, *ARA&A*, **47**, 481
- Badenes C., et al., 2018, *ApJ*, **854**, 147
- Banerjee P., Qian Y.-Z., Heger A., 2018, *ApJ*, **865**, 120
- Battino U., et al., 2016, *ApJ*, **827**, 30
- Beers T. C., Christlieb N., 2005, *ARA&A*, **43**, 531
- Biermann L., 1932, *Z. Astrophys.*, **5**, 117
- Bisterzo S., Gallino R., Straniero O., Cristallo S., Käppeler F., 2012, *MNRAS*, **422**, 849
- Blöcker T., 1995, *A&A*, **297**, 727
- Busso M., Gallino R., Lambert D. L., Travaglio C., Smith V. V., 2001, *ApJ*, **557**, 802
- Campbell S. W., Lugaro M., Karakas A. I., 2010, *A&A*, **522**, L6
- Cassisi S., Iben Jr. I., Tornambè A., 1998, *ApJ*, **496**, 376
- Chen M. C., Herwig F., Denissenkov P. A., Paxton B., 2014, *MNRAS*, **440**, 1274
- Churazov E., et al., 2014, *Nature*, **512**, 406
- Clarkson O., Herwig F., Pignatari M., 2018, *MNRAS*, **474**, L37
- Clayton D. D., 1968, *Principles of stellar evolution and nucleosynthesis*. New York: McGraw-Hill
- Colella P., Woodward P. R., 1984, *Journal of Computational Physics*, **54**, 174
- Côté B., Denissenkov P., Herwig F., Ruiter A. J., Ritter C., Pignatari M., Belczynski K., 2018, *ApJ*, **854**, 105
- Cowan J. J., Rose W. K., 1977, *ApJ*, **212**, 149
- Cyburt R. H., et al., 2010, *ApJS*, **189**, 240
- Dardelet L., et al., 2015, preprint, ([arXiv:1505.05500](https://arxiv.org/abs/1505.05500))
- Denissenkov P. A., 2010, *ApJ*, **723**, 563
- Denissenkov P. A., Pinsonneault M., 2008, *ApJ*, **679**, 1541
- Denissenkov P. A., Herwig F., Battino U., Ritter C., Pignatari M., Jones S., Paxton B., 2017a, *ApJ*, **834**, L10
- Denissenkov P. A., VandenBerg D. A., Kopacki G., Ferguson J. W., 2017b, *ApJ*, **849**, 159
- Denissenkov P., et al., 2018, *Journal of Physics G Nuclear Physics*, **45**, 055203
- Fuhrmann K., Chini R., Kaderhandt L., Chen Z., 2017, *ApJ*, **836**, 139
- Hempel M., Stancliffe R. J., Lugaro M., Meyer B. S., 2016, *ApJ*, **831**, 171
- Han Z., Podsiadlowski P., 2004, *MNRAS*, **350**, 1301
- Herwig F., 2000, *A&A*, **360**, 952
- Herwig F., 2005, *Annu. Rev. Astro. Astrophys.*, **43**, 435
- Herwig F., Blöcker T., Schoenberner D., El Eid M., 1997, *A&A*, **324**, L81
- Herwig F., Freytag B., Fuchs T., Hansen J. P., Hueckstaedt R. M., Porter D. H., Timmes F. X., Woodward P. R., 2007, in Kerschbaum F., Charbonnel C., Wing R. F., eds, *Astronomical Society of the Pacific Conference Series Vol. 378, Why Galaxies Care About AGB Stars: Their Importance as Actors and Probes*. p. 43 ([arXiv:0709.0197](https://arxiv.org/abs/0709.0197))
- Herwig F., Pignatari M., Woodward P. R., Porter D. H., Rockefeller G., Fryer C. L., Bennett M., Hirschi R., 2011, *ApJ*, **727**, 89
- Herwig F., Woodward P. R., Lin P.-H., Knox M., Fryer C., 2014, *ApJ*, **792**, L3
- Hillebrandt W., Niemeyer J. C., 2000, *ARA&A*, **38**, 191
- Hillebrandt W., Kromer M., Röpke F. K., Ruiter A. J., 2013, *Frontiers of Physics*, **8**, 116
- Hoyle F., Fowler W. A., 1960, *ApJ*, **132**, 565
- Idan I., Shaviv N. J., Shaviv G., 2013, *MNRAS*, **433**, 2884
- Iwamoto N., Kajino T., Mathews G. J., Fujimoto M. Y., Aoki W., 2004, *ApJ*, **602**, 377
- Johnson J. A., Bolte M., 2004, *ApJ*, **605**, 462
- Jones S., Ritter C., Herwig F., Fryer C., Pignatari M., Bertolli M. G., Paxton B., 2016, *MNRAS*, **455**, 3848
- Jones S., Andrassy R., Sandalski S., Davis A., Woodward P., Herwig F., 2017, *MNRAS*, **465**, 2991
- Lepo K., van Kerkwijk M., 2013, *ApJ*, **771**, 13
- Livio M., Mazzali P., 2018, preprint, ([arXiv:1802.03125](https://arxiv.org/abs/1802.03125))
- Lugaro M., Karakas A. I., Stancliffe R. J., Rijs C., 2012, *ApJ*, **747**, 2
- Masseron T., Johnson J. A., Plez B., van Eck S., Primas F., Goriely S., Jorissen A., 2010, *A&A*, **509**, A93
- Moe M., Kratter K. M., Badenes C., 2019, *ApJ*, **875**, 61
- Müller B., Janka H.-T., 2015, *MNRAS*, **448**, 2141
- Nomoto K., 1982, *ApJ*, **253**, 798
- Nomoto K., Saio H., Kato M., Hachisu I., 2007, *ApJ*, **663**, 1269
- Paxton B., Bildsten L., Dotter A., Herwig F., Lesaffre P., Timmes F., 2011, *ApJS*, **192**, 3
- Paxton B., et al., 2013, *ApJS*, **208**, 4
- Piersanti L., Tornambè A., Yungelson L. R., 2014, *MNRAS*, **445**, 3239
- Pignatari M., et al., 2016, *ApJS*, **225**, 24
- Porter D. H., Woodward P. R., 2000, *ApJS*, **127**, 159
- Postnov K. A., Yungelson L. R., 2014, *Living Reviews in Relativity*, **17**, 3
- Schatzman E., 1963, in Gratton L., ed., *Star Evolution*. p. 389
- Spruit H. C., 2015, *A&A*, **582**, L2
- Stancliffe R. J., Glebbeek E., Izzard R. G., Pols O. R., 2007, *A&A*, **464**, L57
- Wang B., 2018, *Research in Astronomy and Astrophysics*, **18**, 049
- Wang B., Li Y., Ma X., Liu D.-D., Cui X., Han Z., 2015, *A&A*, **584**, A37
- Werner K., Herwig F., 2006, *PUBL ASTRON SOC PAC*, **118**, 183
- Whelan J., Iben Jr. I., 1973, *ApJ*, **186**, 1007
- Wolf W. M., Bildsten L., Brooks J., Paxton B., 2013, *ApJ*, **777**, 136
- Woods T. E., Gilfanov M., 2016, *MNRAS*, **455**, 1770
- Woodward P. R., 1986, in Winkler K.-H. A., Norman M. L., eds, *NATO Advanced Science Institutes (ASI) Series C Vol. 188*, NATO Advanced Science Institutes (ASI) Series C. p. 245
- Woodward P. R., 2007, in Grinstein F. F., Margolin L. G., Rider W. J., eds, *Implicit Large Eddy Simulation, Computing Turbulent Fluid Dynamics*. Cambridge University Press, Cambridge, p. 130
- Woodward P., Colella P., 1981, in W. C. Reynolds and R. W. McCormack ed., *Lecture Notes in Physics*. Springer Verlag, Berlin, pp 434–441
- Woodward P., Colella P., 1984, *Journal of Computational Physics*, **54**, 115
- Woodward P. R., Herwig F., Lin P.-H., 2015, *ApJ*, **798**, 49
- van den Heuvel E. P. J., Bhattacharya D., Nomoto K., Rappaport S. A., 1992, *A&A*, **262**, 97

APPENDIX A: THE IMPLEMENTATION OF MASS INGESTION IN RAWD MODELS

Let us denote X_i^k and X_o^k the mass fractions of the k th isotope, respectively, inside and outside the convective He shell, in the vicinity of its outer boundary. We assume that the envelope matter ingested into the He shell gets immediately distributed within an ingestion zone with the mass $\Delta M \ll M_{\text{top}} - M_{\text{bot}}$, where M_{bot} and M_{top} are the mass coordinates of the bottom and the top of the He shell. The input parameters here are X_o^k , ΔM , and the mass ingestion

rate \dot{M}_{ing} . Because of a small size of the ingestion zone, we assume that all the isotopes are linearly distributed in it, i.e.

$$X_i^k(M) = X_i^k(M_{\text{max}}) - \frac{(M_{\text{max}} - M)}{\Delta M} [X_i^k(M_{\text{max}}) - X_i^k(M_{\text{min}})],$$

where $M_{\text{min}} \leq M \leq M_{\text{max}}$, $M_{\text{max}} = M_{\text{top}}$, and $M_{\text{min}} = M_{\text{max}} - \Delta M$. The total mass of the k th isotope in this distribution is

$$\Delta M_i^k = \int_{M_{\text{min}}}^{M_{\text{max}}} X_i^k(M) dM = \frac{1}{2} [X_i^k(M_{\text{min}}) + X_i^k(M_{\text{max}})] \Delta M.$$

After $\Delta M_{\text{ing}} = \dot{M}_{\text{ing}} \Delta t$ of the envelope matter is ingested, the mass of the k th isotope in the ingestion zone becomes

$$\widetilde{\Delta M_i^k} = \Delta M_i^k + X_o^k \Delta M_{\text{ing}} - \delta M_i^k,$$

where

$$\begin{aligned} \delta M_i^k &= \int_{M_{\text{max}} - \Delta M_{\text{ing}}}^{M_{\text{max}}} X_i^k(M) dM = X_i^k(M_{\text{max}}) \Delta M_{\text{ing}} \\ &+ \frac{1}{2} \frac{\Delta M_{\text{ing}}^2}{\Delta M} [X_i^k(M_{\text{min}}) - X_i^k(M_{\text{max}})] \end{aligned}$$

is the mass of the k th isotope in the mass ΔM_{ing} that replaces the ingested mass outside the He shell (we assume that the mixing between the He shell and the envelope does not change the chemical composition, X_o^k , of the latter.)

The change of the average mass fraction of the k th isotope in the ingestion zone is therefore

$$\begin{aligned} \Delta \langle X_i^k \rangle &= \frac{\widetilde{\Delta M_i^k}}{\Delta M} - \frac{\Delta M_i^k}{\Delta M} = [X_o^k - X_i^k(M_{\text{max}})] \frac{\Delta M_{\text{ing}}}{\Delta M} \\ &+ \frac{1}{2} [X_i^k(M_{\text{max}}) - X_i^k(M_{\text{min}})] \left(\frac{\Delta M_{\text{ing}}}{\Delta M} \right)^2. \end{aligned}$$

This change can be applied either as a step increase of the previous linear distribution

$$\widetilde{X_i^k(M)} = X_i^k(M) + \Delta \langle X_i^k \rangle,$$

or as a ramp increase

$$\widetilde{X_i^k(M)} = X_i^k(M) + 2 \frac{(M - M_{\text{min}})}{\Delta M} \Delta \langle X_i^k \rangle$$

for $M_{\text{min}} \leq M \leq M_{\text{max}}$. In the present work, we have chosen the latter option.

This paper has been typeset from a \LaTeX file prepared by the author.